Biomaterials Science

ROYAL SOCIETY OF CHEMISTRY

PAPER

View Article Online
View Journal | View Issue

Cite this: *Biomater. Sci.*, 2026, **14**, 2730

MOF-based arginine nanocarriers for coordinated immunometabolic and antitumor modulation in triple negative breast cancer

Amir M. Alsharabasy, *[a] Aibhe Boran, [b] Roberto González-Gómez,[b] Harry Revill,[a] Abhay Pandit[a] and Pau Farràs*[a,b]

L-Arginine (L-Arg) is a key immunometabolite and nitric oxide (•NO) precursor with therapeutic potential in cancer and immunotherapy. However, its clinical application is hindered by poor bioavailability and uncontrolled dosing. Here, two distinct metal–organic frameworks (MOFs), NH_2-MIL-125(Ti) and MOF-808(Zr), were engineered as nanocarriers for L-Arg to enable coordinated tumour–immune modulation in triple-negative breast cancer (TNBC). L-Arg loading and release were systematically characterized, followed by Seahorse metabolic flux, flow cytometry, live-cell imaging, and wound healing assays to evaluate biological effects in activated human T cells and inducible nitric oxide synthase (iNOS)-transduced MDA-MB-231 cells. Both MOFs demonstrated successful L-Arg encapsulation with distinct release kinetics. In activated $CD4^+$ T cells, Arg-loaded MOFs induced profound metabolic reprogramming independent of detectable •NO production. MOF-808-Arg enhanced oxidative phosphorylation and preserved spare respiratory capacity, while NH_2-MIL-125-Arg triggered hypermetabolism characterized by elevated proton leak and loss of respiratory reserve, mimicking high-dose L-Arg stress. In contrast, in iNOS-expressing MDA-MB-231 cells, both MOFs increased intracellular •NO levels, resulting in reduced viability and inhibited migration. These findings demonstrate that controlled arginine delivery exerts dual and context-dependent effects, coupling •NO-mediated tumour cytotoxicity with •NO-independent enhancement of T-cell metabolic fitness. Overall, this work establishes MOF-based nutrient delivery as a strategy that integrates redox-based gasotransmitter therapy with immunometabolic reprogramming, highlighting the importance of carrier-dependent release kinetics in shaping both tumour and immune cell responses in metabolically hostile cancers such as TNBC.

Received 10th February 2026,
Accepted 18th April 2026

DOI: 10.1039/d6bm00195e

rsc.li/biomaterials-science

1. Introduction

Nitric oxide (•NO) is a key endogenous gasotransmitter produced by nitric oxide synthases (NOS), with established roles in vasodilation, neurotransmission, and immune defence.[1,2] In cancer, however, dysregulated •NO signalling can promote tumour progression, angiogenesis, and metastatic dissemination.[3–5] In triple-negative breast cancer (TNBC), inducible NOS (iNOS) is often overexpressed, and elevated •NO has been linked to activation of pro-tumour pathways, including epidermal growth factor receptor/extracellular signal-regulated kinase (EGFR/ERK) and nuclear factor kappa B (NF-κB), thereby promoting invasion and metastasis.[6–8] Sustained or spatially uncontrolled •NO can also disrupt protein function and promote epithelial–mesenchymal transition,[9] At the same time, •NO may exert anti-tumour effects under specific conditions, including suppression of cell motility and normalization of tumour vasculature.[10,11] This concentration- and context-dependent duality highlights the need for controlled, localized strategies for modulating •NO levels within the tumour microenvironment (TME).[12] To achieve this, diverse •NO-delivery strategies have been explored (*e.g.* diazeniumdiolates, nitrosothiols, metal–nitrosyls, photoactive hydrogels) that release •NO in the tumour microenvironment. However, many synthetic •NO donors (*e.g.* diazeniumdiolates or nitrosothiols) suffer from burst release kinetics, systemic off-target effects, and limited responsiveness to tumour-specific cues.[13,14]

As an alternative, L-arginine (L-Arg), the endogenous substrate of NOS, enables enzyme-mediated and context-dependent •NO generation. Supplementation with L-Arg can markedly elevate intracellular •NO levels, a phenomenon termed the

[a]*CÚRAM, Research Ireland Centre for Medical Devices, University of Galway, H91 W2TY, Ireland. E-mail: amir.abdo@universityofgalway.ie, pau.farras@universityofgalway.ie*
[b]*School of Biological and Chemical Sciences, Ryan Institute, University of Galway, H91 TK33, Ireland*

"L-arginine paradox", even when extracellular arginine appears sufficient.[15–17] In arginine-deprived tumours, particularly those enriched in myeloid arginase activity, restoring L-Arg availability can enhance •NO production and sensitize tumour cells to oxidative stress.[18,19] By restoring arginine levels, one can not only fuel •NO generation but also reinvigorate tumour-infiltrating T cells, improving their survival and anti-tumour activity.[20] Hence, L-Arg delivery allows more controlled, enzyme-mediated •NO production *in situ*.[21]

Beyond conventional drug delivery, growing evidence shows that biomaterials can actively reprogram T-cell metabolism. Amino acid availability, particularly arginine, strongly influences T-cell mitochondrial function, survival, and effector differentiation. Elevating intracellular L-Arg enhances oxidative phosphorylation and spare respiratory capacity in activated T cells, thereby improving persistence and antitumour function. Importantly, these metabolic effects can occur without measurable increases in •NO production, indicating that arginine-mediated T-cell reprogramming may proceed largely independently of canonical NO signalling.[20] Thus, arginine delivery may exert dual effects within tumours: enhancing •NO-driven cytotoxicity in iNOS-expressing cancer cells while simultaneously promoting metabolic fitness in T cells.

Metal–organic frameworks (MOFs) are attractive candidates for such applications because of their high porosity, tuneable surface chemistry, and controllable cargo release.[22,23] Different MOF-based systems have been engineered for chemotherapeutic delivery, induction of immunogenic cell death, and tumour microenvironment modulation. For example, transferrin-functionalized Zn-MOFs improved tumour targeting in TNBC models,[24] while pH-sensitive zeolitic imidazolate framework-8 (ZIF-8) composites co-delivered chemotherapeutic and epigenetic agents to convert immune-"cold" tumours into inflamed phenotypes.[25] MOFs have also been explored as immunomodulatory platforms for delivering antigens, adjuvants, and metabolic regulators to shape antitumour immunity. However, direct enhancement of T-cell metabolic fitness through MOF-mediated nutrient delivery remains largely unexplored.

Among these platforms, zirconium- and titanium-based MOFs, including MOF-808 and NH_2-MIL-125(Ti), are particularly attractive because of their structural stability, biocompatibility, and tunable defect chemistry. MOF-808, constructed from Zr_6-oxo clusters, contains large hexagonal pores (~1.8 nm) and shows high defect tolerance, enabling substantial cargo loading.[26,27] In parallel, NH_2-MIL-125(Ti), built from Ti_8O clusters, exhibits a cage-like porous architecture with high surface area (>1500 $m^2\ g^{-1}$) and pendant amine groups that facilitate hydrogen bonding, electrostatic interactions, and pH-responsive release.[28,29] Despite these favourable properties, a systematic comparison of these frameworks as arginine delivery platforms for linked redox-based tumour targeting and T-cell metabolic modulation has not been reported.

Here, NH_2-MIL-125(Ti) and MOF-808(Zr) were developed and compared as tuneable nanocarriers for localized L-Arg delivery in TNBC. We hypothesize that controlled arginine release can simultaneously (i) amplify intracellular •NO generation in iNOS-expressing TNBC cells to induce cytotoxic and anti-migratory effects, and (ii) enhance mitochondrial respiration and metabolic fitness in activated human T cells. By integrating materials characterization, release kinetics, redox biology, and Seahorse metabolic profiling, we establish a dual-function framework that couples tumour-directed gas-based therapy with immune metabolic support. This work positions MOF-mediated arginine delivery not merely as a •NO amplification strategy, but as a platform for coordinated tumour–immune metabolic modulation within the TNBC microenvironment. An overview of the study design is presented in Scheme 1.

2. Materials and methods

2.1. Materials and reagents

Titanium isopropoxide (TTIP), 2-aminoterephthalic acid (NH_2-BDC), zirconyl chloride octahydrate ($ZrOCl_2{\cdot}8H_2O$), 1,3,5-benzenetricarboxylic acid (trimesic acid, BTC), formic acid, L-Arg, ninhydrin (25 mg mL^{-1}), hydrindantin, equine heart myoglobin, anhydrous dimethyl sulphide (DMSO), calibration standards for Ti (#43843) and Zr (#51244), BODIPY™ 581/591 C11 dye, phosphate-buffered saline (PBS), RPMI-1640 medium, L-glutamine, penicillin/streptomycin, poly-L-lysine (PLL), fetal bovine serum (FBS) were all purchased from Sigma-Aldrich. *N*,*N*-Dimethylformamide (DMF), methanol, hydrochloric acid, dichloromethane (DCM), sodium hydroxide, Cell-Quant alamarBlue™ Cell Viability Reagent, Invitrogen Griess reagent kit, Invitrogen 4-Amino-5-ethylamino-2′,7′-difluorofluorescein diacetate (DAF-FM), human interleukin-2 (IL-2), anti-CD3/CD28 Dynabeads, human interferon gamma (IFN-É£) Uncoated ELISA Kit (#88-7316-88), and Nunc™ 96-well optical-bottom black microplates were obtained from Fisher Scientific. Lymphoprep™ (#18061) and SepMate™ (#85450) were from STEMCELL, Germany, CD4+ T Cell Isolation Kit, (human, #130-096-533) was from Miltenyi Biotec, Germany. Zombie Red™ Fixable Viability kit (#423109) was from BioLegend. Seahorse XF Cell Mito Stress Test Kits, XFp cell culture microplates, and sensor cartridges were purchased from Agilent Technologies.

2.2. Materials synthesis and physicochemical characterisation

2.2.1. Synthesis of NH_2-MIL-125. NH_2-MIL-125(Ti) nanoparticles were synthesized *via* a solvothermal method adapted from the literature.[30] 2-Aminoterephthalic acid (NH_2-BDC) was dissolved in a mixture of DMF and methanol, followed by the addition of a titanium alkoxide precursor, titanium isopropoxide (TTIP). The resulting mixture was stirred vigorously for approximately 1 h to ensure homogeneity before being transferred to a Teflon-lined autoclave. The solvothermal reaction was carried out at a temperature between 140 and 150 °C for 15–28 h. After naturally cooling to room temperature, the resulting yellow solid was collected and purified by sequential washing with DMF and methanol to remove unreacted species

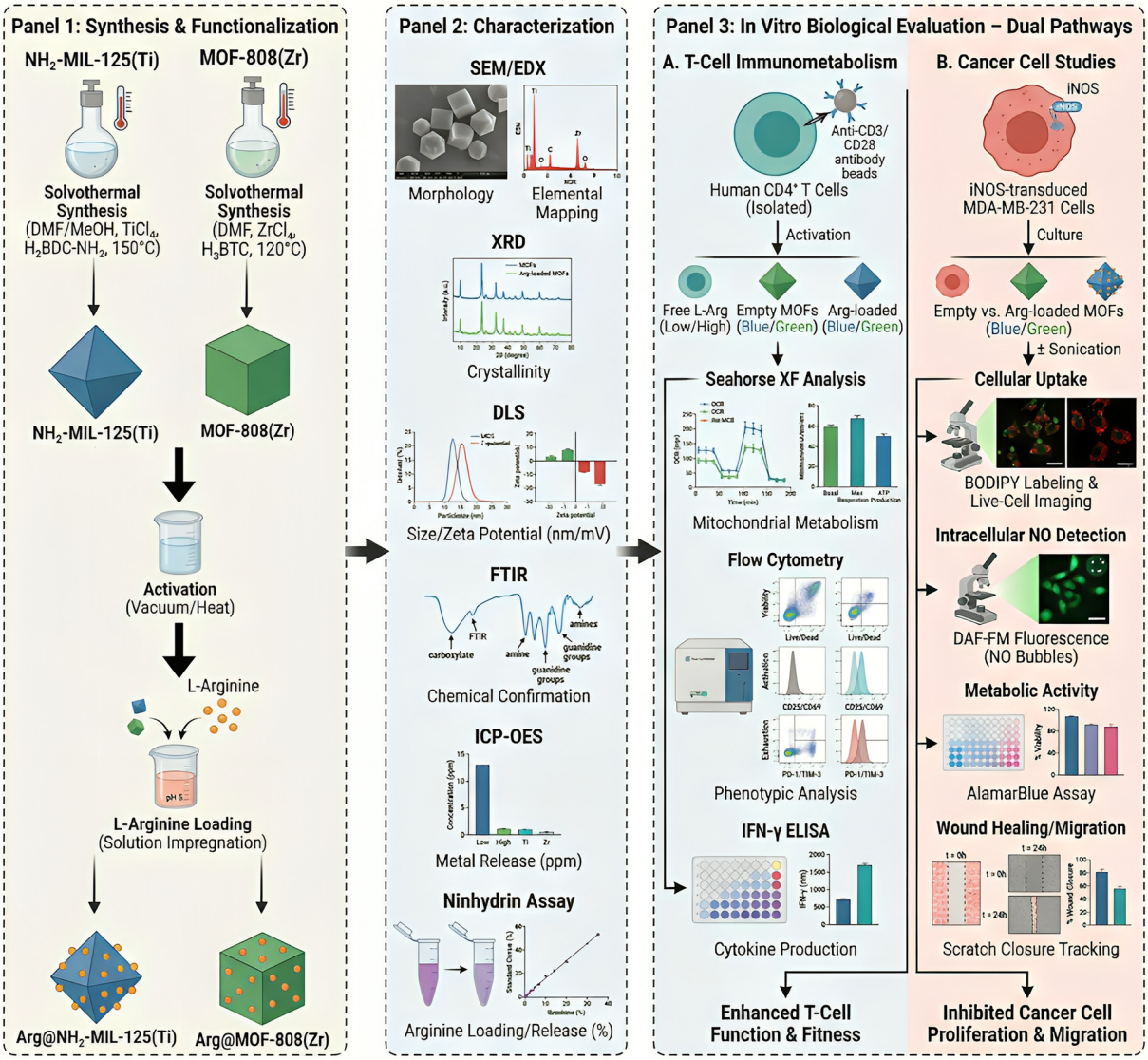

Scheme 1 Schematic overview of the synthesis, characterization, and biological evaluation of L-arginine-loaded MOF nanocarriers for immunometabolic and antitumor modulation in TNBC. Created by illustrae.co.

and residual solvents. The final product was obtained as a yellow powder by drying under vacuum at 85–100 °C.

2.2.2. Synthesis of MOF-808. MOF-808 was synthesized *via* a modified solvothermal method based on a previously reported procedure.[31] Briefly, $ZrOCl_2{\cdot}8H_2O$ (0.3 mmol) and BTC (0.4 mmol) were dissolved in a solvent mixture of DMF (5 mL) and formic acid (5 mL). The reaction mixture was heated at 100 °C for 18 h, yielding a white precipitate. The product was collected and washed sequentially with DMF and methanol to remove the unreacted precursors.

2.2.3. Synthesis of arginine (Arg)-loaded MOFs. The NH_2-MIL-125(Ti) and MOF-808 particles were activated by immersion in dry DCM overnight, followed by centrifugation (10 000 rpm, 10 min) and subsequent activation under dynamic vacuum at 150 °C overnight. L-Arg loading was performed using a solution-based impregnation method.[32] Typically, 30 mg of activated MOFs was dispersed in 30 mL of deionized water and sonicated for 30 min to form a homogeneous suspension. A 7.5 mL aliquot of a freshly prepared L-Arg aqueous solution (2 mg mL^{-1}) was added dropwise to the dispersion of the nanoparticles. The pH of the mixture was adjusted to 5.5 and stirred overnight at room temperature to facilitate adsorption. The product was then collected by centrifugation (10 000 rpm, 10 min) and thoroughly washed with deionized water to remove unbound amino acids. The final L-Arg-loaded MOFs were obtained as dry powders after freeze-drying for 24 h. For comparison, L-Arg was loaded into nonactivated, as-synthesized MOFs following the same procedure.

2.2.4. Characterization of the synthesized MOFs. Characterisation was performed using a comprehensive suite of analytical techniques. Particle morphology and elemental composition were examined by scanning electron microscopy

(SEM; Hitachi S-2600TM and S-4700) coupled with energy-dispersive X-ray spectroscopy (EDX), following sputter-coating with a thin gold layer to ensure electrical conductivity. Crystallinity was assessed by powder X-ray diffraction (PXRD) using an Aeris diffractometer equipped with a Cu Kα radiation source. Chemical functionality was analysed by Fourier-transform infrared (FTIR) spectroscopy (Shimadzu IRSpirit), with spectra acquired over the range 500–4000 cm^{-1} at a resolution of 4 cm^{-1} and averaged over 128 scans.

Hydrodynamic particle size and zeta potential were measured by dynamic light scattering (DLS) using a Litesizer™ 500 (Anton Paar) at 25 °C. Samples were dispersed in PBS or PBS supplemented with 10% FBS at a concentration of 100 μg mL^{-1}, probe-sonicated for 20 s, and analysed using appropriate cuvettes (refractive index 1.37 for size measurements and 1.33 for zeta potential). Results are reported as the mean of five independent replicates, with 60 runs per measurement.

For degradation studies, MOF nanoparticles were suspended in PBS at 100 μg mL^{-1}, briefly sonicated, and incubated under shaking conditions at 37 °C for up to 36 h. At predefined time points, aliquots were collected, centrifuged at 15 000*g* for 20 min, and the supernatants were diluted in 2% nitric acid. The concentrations of Zr and Ti released from the respective MOFs were quantified using an Agilent 5110 inductively coupled plasma–optical emission spectrometer (ICP–OES), with data processed using ICP Expert software (version 7.4.1.10449).

2.2.5. Quantification of arginine loading and release. A ninhydrin-based colorimetric assay was employed to quantify L-Arg loading capacity, loading efficiency, and release kinetics of MOF carriers. Aliquots collected during successive washing and purification steps of the L-Arg-loaded MOFs were analysed, and the remaining L-Arg concentration was compared with that of the initial loading solution. For the release studies, L-Arg-loaded MOFs (100 μg mL^{-1}) were dispersed in either PBS or a 1 : 1 (v/v) FBS/PBS mixture, briefly sonicated (20 s), and maintained at 37 °C under gentle agitation. At predetermined time points (1, 2, 4, 8, 12, 24, and 48 h), 70 μL aliquots were withdrawn and immediately centrifuged (8000*g*, 10 min) to remove particulates. Arginine concentrations in the supernatants were determined using the optimized ninhydrin protocol described before.[33] The reagent was freshly prepared and contained ninhydrin (25 mg mL^{-1}) and hydrindantin (1 mg mL^{-1}) in a 1 : 1 (v/v) mixture of DMSO and aqueous acetate buffer (2 M acetic acid, 1 M potassium acetate). For each measurement, 50 μL of sample was mixed with 200 μL of reagent, incubated at 90 °C for 45 min, cooled for 15 min, diluted with 1250 μL of 2-propanol/water (1 : 1, v/v), and the absorbance was measured at 570 nm using a microplate reader (Varioskan Flash, Thermo Fisher Scientific, Finland). Aliquots collected from PBS release studies were diluted and analysed using the ninhydrin assay under identical aqueous reaction conditions as the calibration standards. Background absorbance from PBS was corrected using corresponding blank controls. A small but consistent baseline difference between PBS and water was observed and accounted for during data processing, ensuring accurate quantification of L-Arg.

2.3. T-Cell isolation and functional assays

2.3.1. $CD4^+$ T-cell isolation and culture. Whole blood was obtained from University of Galway Hospital following institutional ethical approval. All experiments were performed in accordance with the guidelines of the Declaration of Helsinki and approved by the Research Ethics Committee of the University of Galway. Peripheral blood samples were collected from healthy donors *via* the same hospital, and informed consent was obtained from all participants. Peripheral blood mononuclear cells (PBMCs) were isolated by density gradient centrifugation using Lymphoprep™ and SepMate™ tubes according to the manufacturer's instructions. $CD4^+$ T cells were subsequently purified by negative selection using a $CD4^+$ T Cell Isolation Kit. Isolated $CD4^+$ T cells were cultured in complete RPMI medium supplemented with IL-2 in the presence of anti-CD3/CD28 Dynabeads™ at a bead-to-cell ratio of 1 : 2. Cells were maintained at 37 °C in a humidified atmosphere containing 5% CO_2 for 72 h prior to downstream treatments.

2.3.2. MOF and L-Arg treatments. Activated $CD4^+$ T cells were seeded into 24-well plates at a density of 70×10^4 cells per well and treated with the indicated MOF formulations. MOFs were either directly mixed with the suspended cells or administered using transwell inserts to prevent direct particle–cell contact. For comparison, parallel groups were treated with varying concentrations of free L-Arg. After 48 h of treatment, cells were harvested for flow cytometry and Seahorse metabolic analyses, while conditioned media were collected for cytokine quantification.

2.3.3. Assessment of mitochondrial respiration by Seahorse analysis. Cellular metabolic activity was assessed using a Seahorse XFp extracellular flux analyzer (Agilent Seahorse Bioscience). Following treatment, cells were harvested and seeded at a density of 10×10^4 cells per well onto PLL–coated Seahorse XFp cell culture microplates in serum-free, unbuffered RPMI-1640 medium. The assay medium was supplemented with D-glucose (10 mM), L-glutamine (2 mM), and sodium pyruvate (1 mM). Cells were allowed to equilibrate for 1 h at 37 °C in a non-CO_2 incubator prior to analysis. A mitochondrial stress test was then performed by sequential injections of oligomycin (1.4 μM), carbonyl cyanide-4-(trifluoromethoxy) phenylhydrazone (FCCP; 0.5 μM), and a combined rotenone/antimycin A solution (1.4 μM), as previously described.[20]

2.3.4. Nitrite measurements. Following three days of treatment, culture supernatants from each experimental group were collected and centrifuged to remove cellular debris. Total $^{\bullet}NO$ metabolites (nitrite + nitrate) were quantified using the Griess reagent kit according to the manufacturer's instructions. Briefly, nitrate present in the samples was enzymatically reduced to nitrite using nitrate reductase, followed by colorimetric detection of total nitrite *via* the Griess reaction. Absorbance was measured at 548 nm using a microplate reader, and nitrite concentrations were determined by interp-

olation from a sodium nitrite standard curve prepared in the same culture medium matrix. The assay detection limit was approximately 1 μM, and samples below this threshold were considered not detected (ND).

2.3.5. Flow cytometry analysis. $CD4^+$ T-Cells were first stained with Zombie Red™ Fixable Viability kit to exclude non-viable cells. Cells were then incubated with a panel of fluorochrome-conjugated antibodies targeting surface activation and exhaustion markers: CD4-APC (#17-0049-42), CD69-FITC (#MA1-10275), CD366 (T-cell immunoglobulin and mucin-domain containing-3 (TIM-3))-Super Bright™ 436 (#62-3109-42), CD25-Brilliant Violet™ 605 (#406-0257-42), and CD279 (programmed cell death protein 1 (PD-1))-Super Bright™ 780 (#78-9985-82). Following staining and washing, data were acquired using a Northern Lights™ 3000 flow cytometer (Cytek Biosciences). Data analysis was performed using SpectroFlo™ (Cytek Biosciences) and FlowJo v10 software.

2.3.6. Enzyme-linked immunosorbent assay (ELISA). Following treatment of T cells with the different nanoparticle formulations or 500 μM L-Arg, culture supernatants were collected and IFN-γ levels were quantified by ELISA according to the manufacturer's instructions.

2.4. *In vitro* cancer cell studies (iNOS-MDA-MB-231)

2.4.1. Cell culture. MDA-MB-231 cells, transduced with the iNOS gene were a gift from Prof Sharon Glynn, University of Galway, and were maintained in RPMI-1640 medium supplemented with 10% FBS, 1% penicillin/streptomycin, and 2 μg mL^{-1} puromycin at 37 °C with 5% CO_2. The detailed characterization of these transduced cells has been reported previously.[34]

2.4.2. Cell viability assessment. Cell viability was assessed following established protocols.[35] Briefly, MDA-MB-231(iNOS) cells were seeded at a density of 1.5×10^4 cells per well in 96-well plates. After 24 h, the cells were treated with either L-Arg in complete or serum-free medium or with MOF suspensions. A stock solution of L-Arg was prepared in PBS, then freshly prepared in the culture medium and sterilized by filtration, whereas the MOFs were UV-sterilized (Cross-Linker CL-508, UVItec Ltd; 254 nm, 20 min) and suspended in the culture medium with or without subsequent sonication for 45 min. Metabolic activity was quantified using the AlamarBlue™ assay. For testing cell viability, cells were cultured in Nunc™ 96-well optical-bottom black microplates, stained with 2 μM EthD-1 and 1 μM calcein AM in PBS, and imaged using an Operetta high-content imaging system (PerkinElmer).

2.4.3. Cellular uptake imaging. MOF nanoparticles were initially dispersed in absolute ethanol at a concentration of 1 mg mL^{-1} and incubated with a freshly prepared solution of BODIPY™ 581/591 C11 to achieve a final dye concentration of 10 μg mL^{-1}. The suspension was gently mixed at room temperature for 24 h to allow dye adsorption within or onto the MOF particles. Unbound dye was removed by three successive washing steps with ethanol, followed by centrifugation. The purified BODIPY-loaded nanoparticles were then resuspended in PBS and incubated at 37 °C for 1 h to ensure equilibration and stable dispersion. The loading and release of BODIPY during the successive washing steps were quantified by fluorescence measurements using an excitation wavelength of 581 nm and an emission wavelength of 595 nm. Subsequently, nanoparticles were collected and re-dispersed in either FBS-free or FBS-containing cell culture medium at the desired working concentration. iNOS-transduced MDA-MB-231 cells were treated with the nanoparticle suspensions under standard culture conditions. Live-cell imaging was performed using an IncuCyte® S3 system over a 24 h period to monitor nanoparticle uptake and intracellular fluorescence dynamics. Image acquisition and quantitative analysis of fluorescence intensity and cell response were conducted continuously, with downstream data processing performed as specified.

2.4.4. Measurement of intracellular $^{\cdot}NO$. MDA-MB-231 (iNOS) cells were seeded in 96-well plates using phenol red-free RPMI medium, as described above. After washing with PBS, the cells were loaded with 10 μM DAF-FM in complete medium for 1 h at 37 °C in a 5% CO_2. Following probe removal and washing, the cells were treated with different MOFs prepared as previously described in serum-free, phenol red-free medium, or with varying concentrations of L-Arg. Live-cell imaging was performed every two hours for 48 h using the IncuCyte® S3 system. Fluorescence quantification (green object count/intensity) was automated using the IncuCyte ZOOM software and normalized to the total number of objects per image.

2.4.5. Cell migration assessment. A total of 2.5×10^4 cells were seeded in each well of a sterile 24-well plate containing a silicone insert positioned at the centre of the well and allowed to adhere for 24 h. The inserts were then carefully removed, and the cells were washed with PBS and treated with different frameworks prepared as previously described in phenol red-containing, serum-free RPMI medium and subsequently seeded to transwell inserts. Wound closure was monitored using the IncuCyte® live-cell imaging system, with images captured every three hours over a 48 h period. The wound healing rate was quantified using ImageJ software in combination with the MiToBo toolbox.[36] Three replicates were analysed per group, and the mean values from all measurements were used for analysis.

2.5. Statistical analysis

All experiments were performed with at least three independent replicates unless otherwise specified, and the results are expressed as the mean ± standard deviation (SD) or standard error of means (SEM). For T-cell experiments, biological replicates (n) refer to independent human donors, as indicated in the figure legends. All measurements were performed using cells derived from these donors. For cancer cell assays, n represents independent experiments performed on separate days. Data were analysed using Microsoft Excel and OriginPro software for validation and graphical representation of the results. Statistical significance between groups was determined using a two-tailed Student's t-test for pairwise comparisons as speci-

fied in the figure legends. A p value of <0.05 was considered statistically significant.

3. Results and discussion

3.1. Characterization of synthesized MOF nanoparticles

The synthesized NH_2-MIL-125 and MOF-808 nanoparticles were first characterized to confirm framework formation, morphology, and colloidal behaviour prior to biological evaluation. SEM, EDX, and PXRD analyses verified successful synthesis and preservation of the expected structural features, while DLS and ζ-potential measurements revealed framework-dependent differences in dispersion and serum stability. Detailed physicochemical characterization data are provided in the SI (Fig. S1 and S2).

The colloidal properties of the MOFs were evaluated by dynamic light scattering and ζ-potential measurements under different conditions. Both frameworks exhibited changes in hydrodynamic diameter and surface charge upon activation and arginine loading, reflecting alterations in surface chemistry and interparticle interactions. Notably, MOF-808 showed improved dispersion in serum-containing media, whereas NH_2-MIL-125 displayed a greater tendency toward aggregation. These observations indicate that framework composition and surface chemistry influence colloidal stability in biologically relevant environments. Full datasets and statistical analyses are presented in the SI (Table S1). Collectively, these results confirm the successful synthesis and functionalisation of both MOF platforms, enabling subsequent evaluation of their arginine delivery performance.

3.2 Arginine loading and surface modification

L-Arg was employed as a $^{\bullet}NO$ precursor, exploiting its role as a substrate for iNOS[37,38] to enhance intracellular $^{\bullet}NO$ production in TNBC cells. The controlled delivery of L-Arg *via* MOF carriers was therefore designed to enable localised and sustained $^{\bullet}NO$ generation, amplifying cytotoxic and anti-migratory effects while minimising systemic exposure. The successful incorporation into both MOF frameworks was confirmed by complementary spectroscopic and elemental analyses, without evidence of framework collapse or loss of crystallinity. Changes in surface charge further supported arginine adsorption, indicating interactions between the cationic amino acid and negatively charged framework sites. Detailed FTIR, PXRD, and SEM–EDX data are provided in the SI (Fig. S3, S5 and S6).

Quantitative ninhydrin analysis confirmed these trends, showing that NH_2-MIL-125 exhibited a significantly higher apparent arginine loading capacity (25.32 ± 2.43%) and loading efficiency (50.65 ± 4.87%) than MOF-808 (11.84 ± 1.13% and 23.7 ± 2.26%, respectively). The calibration curve used for arginine quantification is shown in Fig. S7. These results indicate that the Ti-based framework provides a greater number of accessible binding sites for L-Arg under the loading conditions used, whereas the lower loading capacity of MOF-808 is consistent with its comparatively limited structural perturbation following arginine incorporation. Together, these findings show that framework chemistry and activation state critically govern amino-acid loading behaviour, with NH_2-MIL-125 favouring higher arginine uptake and MOF-808 showing improved colloidal stability in biologically relevant media.

To assess framework stability following arginine incorporation, metal ion release was quantified under physiological conditions. The ICP-OES analysis revealed marked differences in titanium release kinetics between bare and Arg-loaded NH_2-MIL-125. Sampling-corrected cumulative release calculations showed minimal Ti leaching at early timepoints (≤10 h) for both materials; however, bare NH_2-MIL-125 exhibited a pronounced Ti burst at 36 h, corresponding to a cumulative release of 29 μg Ti (equivalent to 96 μg mg^{-1} MOF) (Fig. 1A). In contrast, Arg-loaded NH_2-MIL-125 displayed substantially suppressed Ti release over the entire incubation period, reaching only 4.1 μg Ti at 36 h (13.7 μg mg^{-1} MOF). These results indicate that L-Arg loading significantly stabilizes the Ti-oxo framework against hydrolytic degradation, an effect that is not detectable by PXRD alone but becomes evident through solution-phase metal release analysis. However, the cumulative zirconium release profiles revealed markedly different degradation behaviours between unloaded and Arg-loaded MOF-808 nanoparticles (Fig. 1B). Arg-loaded MOF-808 exhibited a pronounced early Zr release, reaching a maximum at the intermediate timepoints, followed by a partial decline and subsequent stabilization at later times. In contrast, unloaded MOF-808 showed consistently low and nearly time-independent Zr release throughout the incubation period, indicating high intrinsic stability of the framework under these conditions. The transient Zr release observed for the Arg-loaded material suggests that Arg incorporation enhances the initial lability of surface-accessible Zr_6-oxo clusters, potentially through competitive coordination or ligand exchange, without inducing sustained framework collapse.

The release behaviour of activated NH_2-MIL-125(Ti)-Arg and MOF-808(Zr)-Arg was next evaluated to determine how framework composition influences arginine retention and diffusion. The two carriers displayed markedly distinct release profiles (Fig. 1C). MOF-808-Arg showed a pronounced initial burst, releasing approximately 19–23 μg mL^{-1} of arginine within the first hour and approaching a plateau of 25–26 μg mL^{-1} by 24 h. In contrast, NH_2-MIL-125-Arg exhibited a slower and more progressive release profile, increasing from 4–6 μg mL^{-1} at 1 h to 17–18 μg mL^{-1} after 24 h, consistent with sustained release. These contrasting release kinetics reflect the distinct structural and chemical features of the two frameworks.

In brief, MOF-808, built from $Zr_6O_4(OH)_4$ clusters bridged by 1,3,5-benzenetricarboxylate linkers, contains large adamantane-like cages (~1.8 nm) and a high internal surface area (>2000 m^2 g^{-1}), which favour rapid diffusion of small, hydrophilic, positively charged L-Arg molecules.[39] Together with the strong hydrolytic stability conferred by Zr–carboxylate coordination bonds,[40,41] this suggests that arginine release from MOF-808 is governed mainly by pore diffusion, with only

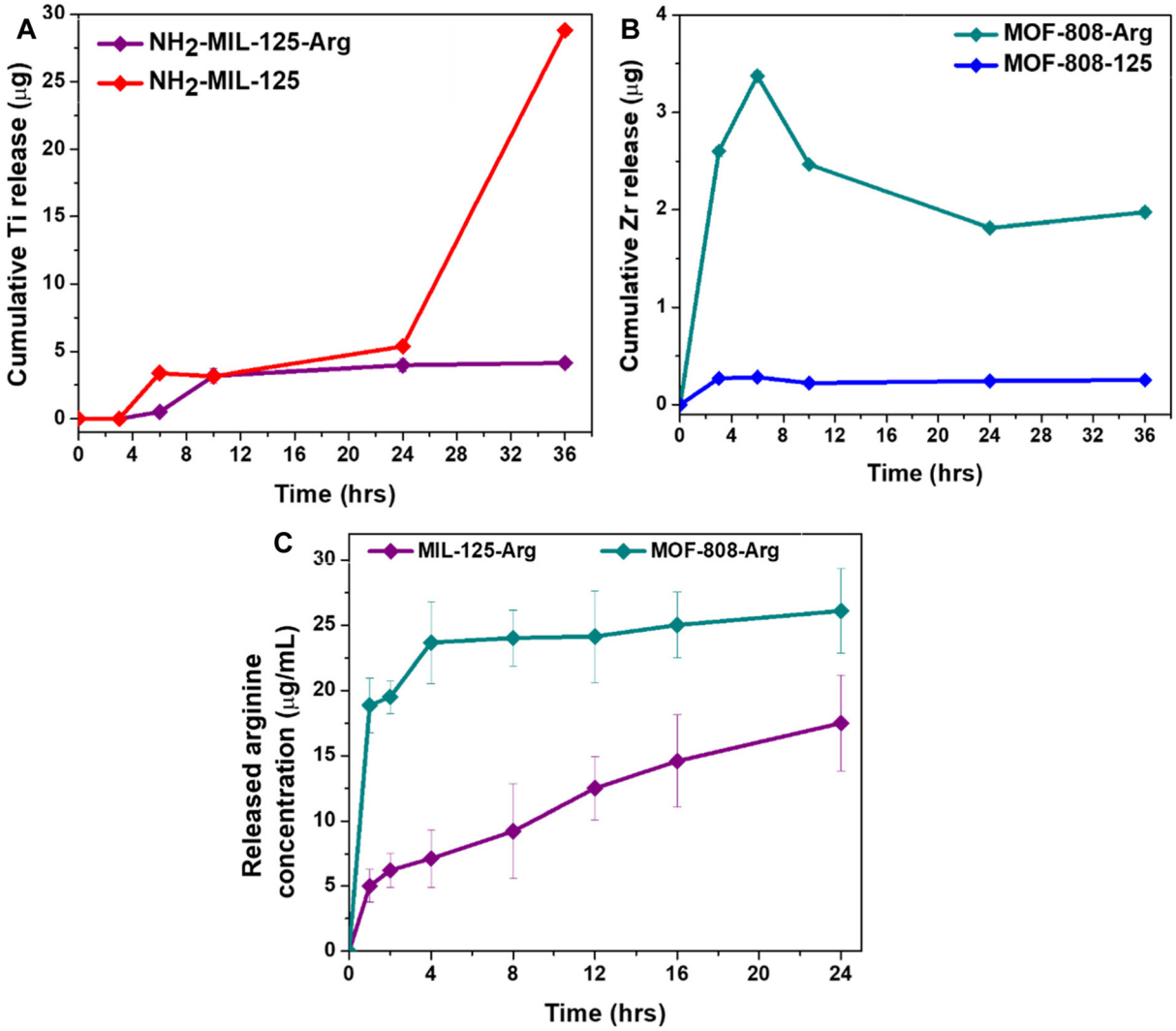

Fig. 1 (A and B) Cumulative Ti and Zr release from activated unloaded and L-Arg-loaded NH_2-MIL-125 and MOF-808 nanoparticles, respectively, in PBS. (C) *In vitro* L-Arg release profiles from activated NH_2-MIL-125-Arg and MOF-808-Arg in PBS at 37 °C, quantified using the ninhydrin colorimetric assay. Data are presented as mean ± SD (n = 3).

limited and transient perturbation of surface-accessible Zr_6 clusters rather than bulk framework degradation. In contrast, NH_2-MIL-125(Ti) possesses narrower pore apertures (~0.6 nm) and Ti–oxo clusters that can engage in hydrogen-bonding and electrostatic interactions with the guanidinium group of L-Arg.[42] These stronger host–guest interactions restrict molecular mobility, resulting in a diffusion-limited release profile without a pronounced initial burst. In addition, the absence of competing anions such as phosphate in the release medium minimises disruption of Ti–carboxylate coordination, further preserving framework integrity and slowing arginine liberation.[43] Accordingly, arginine release from NH_2-MIL-125 proceeds in a more sustained manner through its compact pore network, consistent with the near-linear cumulative release observed over the first 24 h. Collectively, these results indicate that framework-dependent differences in loading capacity and structural lability directly govern arginine release kinetics and provide a mechanistic basis for the distinct biological responses observed for the two MOF systems.

3.3. Immunomodulatory effects of Arg-releasing MOFs on T Cells

3.3.1. Metabolic reprogramming of T cells revealed by Seahorse analysis. To establish a metabolic benchmark for the biomaterial studies, we first examined the effect of soluble L-Arg on mitochondrial respiration in activated human T cells. Seahorse XF analysis showed a clear dose-dependent modulation of oxidative metabolism after 72 h exposure to free arginine (Fig. S8). Relative to untreated cells, 500 μM L-Arg substantially increased basal and maximal oxygen consumption and enhanced adenosine triphosphate (ATP)-linked respiration, consistent with improved oxidative metabolism. In contrast, 2000 μM L-Arg further elevated basal oxygen consumption rate (OCR) but was associated with increased proton leak

and loss of spare respiratory capacity, indicating a shift toward metabolic stress at supraphysiological arginine levels. These findings define a concentration-dependent window in which arginine supports T-cell bioenergetic fitness and provide a reference framework for interpreting the effects of MOF-mediated arginine delivery.

Arg-loaded MOFs induced marked increases in T-cell mitochondrial respiration (Fig. 2A). Basal OCR was significantly elevated in cells treated with Arg-loaded MIL-125 or MOF-808 compared with both untreated cells and cells exposed to unloaded MOFs (Fig. 2B). MIL-125-Arg increased basal respiration by ~4.5-fold relative to untreated T cells and by ~35-fold relative to empty MIL-125, while MOF-808-Arg increased basal OCR by ~3.3-fold *versus* untreated cells. Notably, MIL-125-Arg produced a higher basal OCR than MOF-808-Arg, consistent with the greater L-Arg loading capacity of the Ti-based carrier. In contrast, unloaded MOFs severely suppressed respiration, with basal OCR reduced to 13 ± 2 pmol min^{-1} for MIL-125 and 4 ± 1 pmol min^{-1} for MOF-808, compared with 102 ± 5 pmol min^{-1} in untreated controls. This pronounced impairment is consistent with the known dependence of T-cell bioenergetics on arginine availability.[44,45]

The increase in basal respiration in the Arg-loaded groups translated into substantially higher ATP-linked respiration (Fig. 2C). Following oligomycin injection, both MIL-125-Arg and MOF-808-Arg exhibited ~3.4-fold greater ATP-linked OCR than untreated cells, whereas ATP-linked respiration in the unloaded MOF groups was nearly abolished. Although both Arg-loaded formulations strongly enhanced maximal respiration (Fig. S9B), their respiratory reserve differed markedly: MOF-808-Arg retained substantial spare respiratory capacity, whereas MIL-125-Arg showed essentially none (Fig. 2D). This

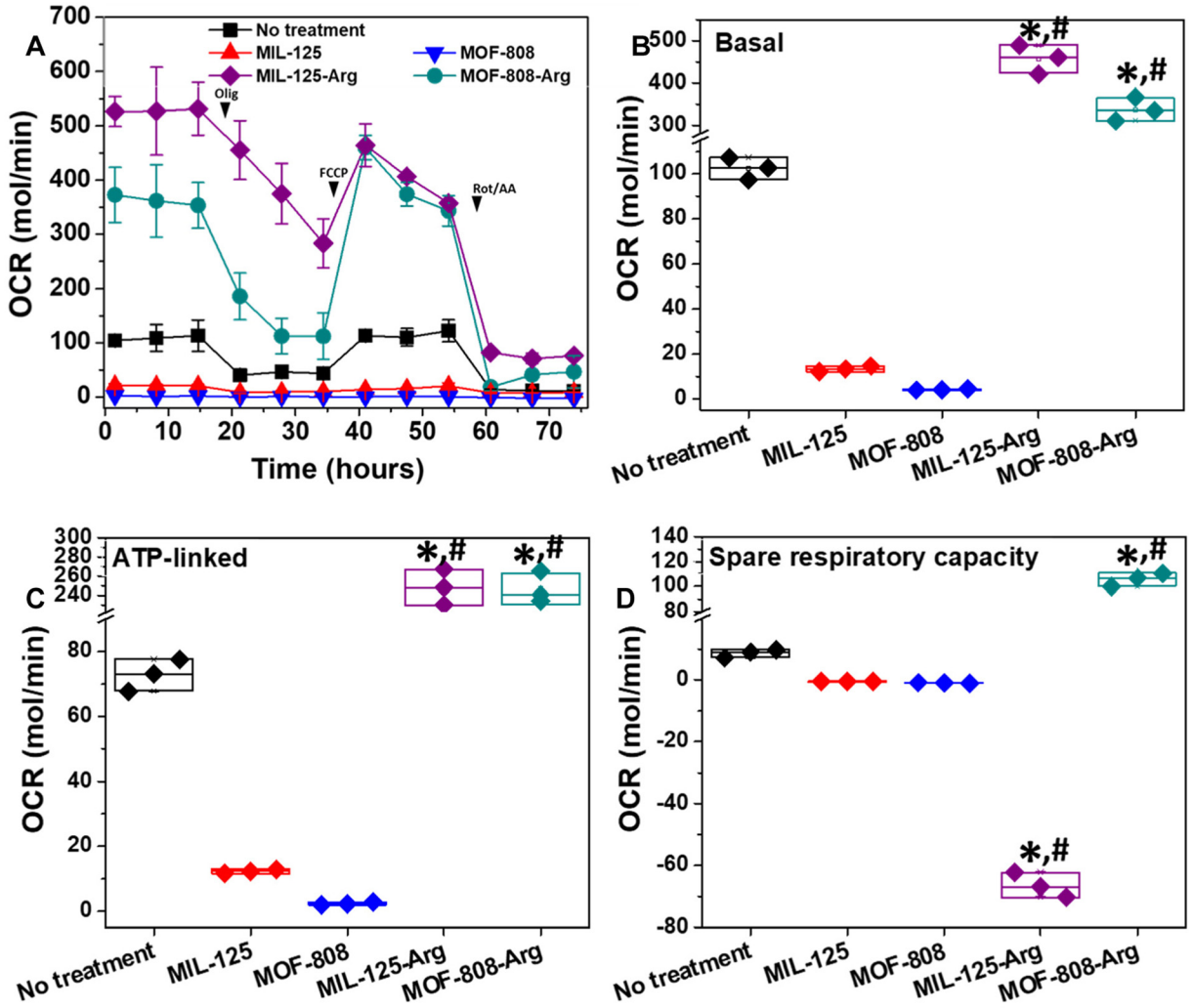

Fig. 2 Arg-loaded MOFs differentially modulate mitochondrial respiration in activated human T cells. (A) Real-time oxygen consumption rate (OCR) profiles of T cells treated with 50 μg mL^{-1} of unloaded and Arg-loaded NH_2-MIL-125 and MOF-808 nanoparticles. (B–D) Quantification of metabolic parameters including basal respiration, ATP production, and spare respiratory capacity. Data are shown for three independent biological donors (n = 3). Each plotted point represents one donor with three technical replicates. Statistical significance was determined using a two-tailed unpaired t-test: *p < 0.05 *versus* untreated control; $^{\#}p$ < 0.05 for Arg-loaded MOF compared to its unloaded counterpart.

indicates that MIL-125-Arg-treated cells were operating close to their maximal respiratory rate under basal conditions.

These differences were reinforced by the proton leak data (Fig. S9C). Oligomycin-resistant OCR rose to 212 ± 25 pmol min^{-1} in MIL-125-Arg-treated cells, compared with 93.6 ± 10 pmol min^{-1} for MOF-808-Arg and 29.6 ± 2 pmol min^{-1} in untreated controls. Thus, although both carriers enhanced mitochondrial activity, MIL-125-Arg induced more than double the proton leak observed with MOF-808-Arg, indicating lower coupling efficiency and a greater fraction of respiration uncoupled from ATP synthesis. This pattern suggests that the sustained arginine exposure associated with MIL-125-Arg drives a hypermetabolic state accompanied by mitochondrial stress, whereas the more rapid release profile of MOF-808-Arg supports enhanced respiration with comparatively lower metabolic inefficiency.

Non-mitochondrial oxygen consumption was also elevated, particularly in the MIL-125-Arg group (Fig. S9D), suggesting activation of extra-mitochondrial oxygen-consuming processes. Parallel nitrite quantification by Griess assay showed no detectable accumulation of NO-derived metabolites across conditions, indicating that $^{\bullet}NO$ production is unlikely to be a dominant driver of the observed metabolic changes. This is consistent with previous reports showing that exogenous L-Arg can enhance T-cell metabolic fitness and survival without measurable $^{\bullet}NO$ production, supporting an immunometabolic rather than $^{\bullet}NO$-dependent mechanism.[20] The elevated non-mitochondrial OCR therefore likely reflects arginine-driven metabolic rewiring, potentially involving arginine-sensing pathways, enhanced biosynthetic activity, and increased demand from other oxygen-consuming processes.

More broadly, the two Arg-loaded MOFs produced metabolic phenotypes resembling different soluble arginine exposure states, highlighting the importance of delivery kinetics in shaping T-cell responses. MOF-808-Arg promoted a more balanced bioenergetic profile, with enhanced respiration but preserved reserve capacity, whereas MIL-125-Arg induced stronger basal activation at the expense of coupling efficiency and respiratory flexibility. These differences are consistent with the faster release profile of MOF-808 and the higher loading capacity and more sustained arginine exposure associated with NH_2-MIL-125, indicating that the immunometabolic effects of MOF-delivered arginine depend not only on total cargo release but also on the extent and duration of cellular exposure.[20,46]

3.3.2. T-Cell viability and activation following MOF treatment. The safety profile of MOF carriers is a key consideration for biomedical application. In activated human T cells, viability and phenotypic marker analyses following exposure to unloaded and Arg-loaded MOFs provided a direct measure of immune-cell compatibility. The use of transwell inserts further indicated that part of the adverse effect of empty nanoparticles was associated with direct particle–cell interactions rather than soluble factors alone.

Following 72 h of treatment, T-cell viability was assessed across all conditions. Untreated cells maintained high viability (~96%), and soluble L-Arg supplementation (0.5–2 mM) had no adverse effect (94–96%; Fig. S10A). In contrast, direct exposure to empty MOF-808 significantly reduced viability to ~82% ($p < 0.05$ *vs.* control), whereas separation by transwell largely mitigated this effect (~91%), indicating that direct particle–cell interaction contributes substantially to toxicity (Fig. 3A). Empty NH_2-MIL-125 showed only a mild, non-significant effect on viability. Importantly, arginine loading improved the tolerability of both carriers, with Arg-loaded MOF-808 restoring viability toward control levels and Arg-loaded NH_2-MIL-125 showing no evident cytotoxicity. This protective effect was less pronounced in the transwell setup (~84% viability), indicating that while arginine release is beneficial, diffusible nanoparticle components may still exert minor negative effects. Arg-loaded MIL-125 did not impair viability. Immunophenotyping revealed a consistently predominant $CD4^+$ population (~98–99% of live cells) across all conditions, with no treatment altering the CD4 : CD8 ratio (Fig. S11A). This confirms that subsequent functional differences are attributable to changes in activation state, not subset composition. The improved cytocompatibility of MOF-808 formulations may also be attributed to its greater colloidal stability in serum-containing media, which reduces aggregation and limits direct particle–cell interactions. In contrast, the comparatively lower stability of NH_2-MIL-125 may promote particle aggregation, contributing to the observed differences in cellular responses.

T-cell activation was further evaluated using the markers CD25 and CD69. Untreated cells were already highly activated, and soluble L-Arg modestly increased CD25 expression. Empty MOF-808 reduced CD25 levels and showed donor-dependent suppression of activation, whereas arginine loading reversed this effect and increased CD25 expression to levels comparable to or greater than control (Fig. 3B). A similar pattern was observed for CD69, with Arg-loaded MOF-808 producing the clearest increase over untreated cells (Fig. 3C). Together, these data indicate that arginine delivery not only improves T-cell viability but also promotes an activated phenotype, particularly in the MOF-808 formulation where loading rescues the adverse effects of the empty carrier.

The exhaustion-associated markers TIM-3 and PD-1 revealed a more nuanced phenotypic response. Soluble L-Arg reduced TIM-3 expression relative to untreated cells, consistent with delayed terminal exhaustion (Fig. 3D). Empty MOF-808 increased TIM-3 in one donor and contributed to a higher group mean, whereas Arg-loaded formulations generally showed lower TIM-3 than their unloaded counterparts. PD-1 displayed a different pattern, with Arg-loaded MOFs often associated with increased expression (Fig. S11B), likely reflecting activation-associated checkpoint induction rather than overt dysfunction. Taken together, these results suggest that arginine delivery promotes activation while limiting later exhaustion-associated features, rather than simply driving uncontrolled T-cell stimulation.

These phenotypic findings are consistent with the Seahorse analysis, which showed that Arg-loaded MOFs restore oxidative metabolism in activated T cells, whereas empty carriers sup-

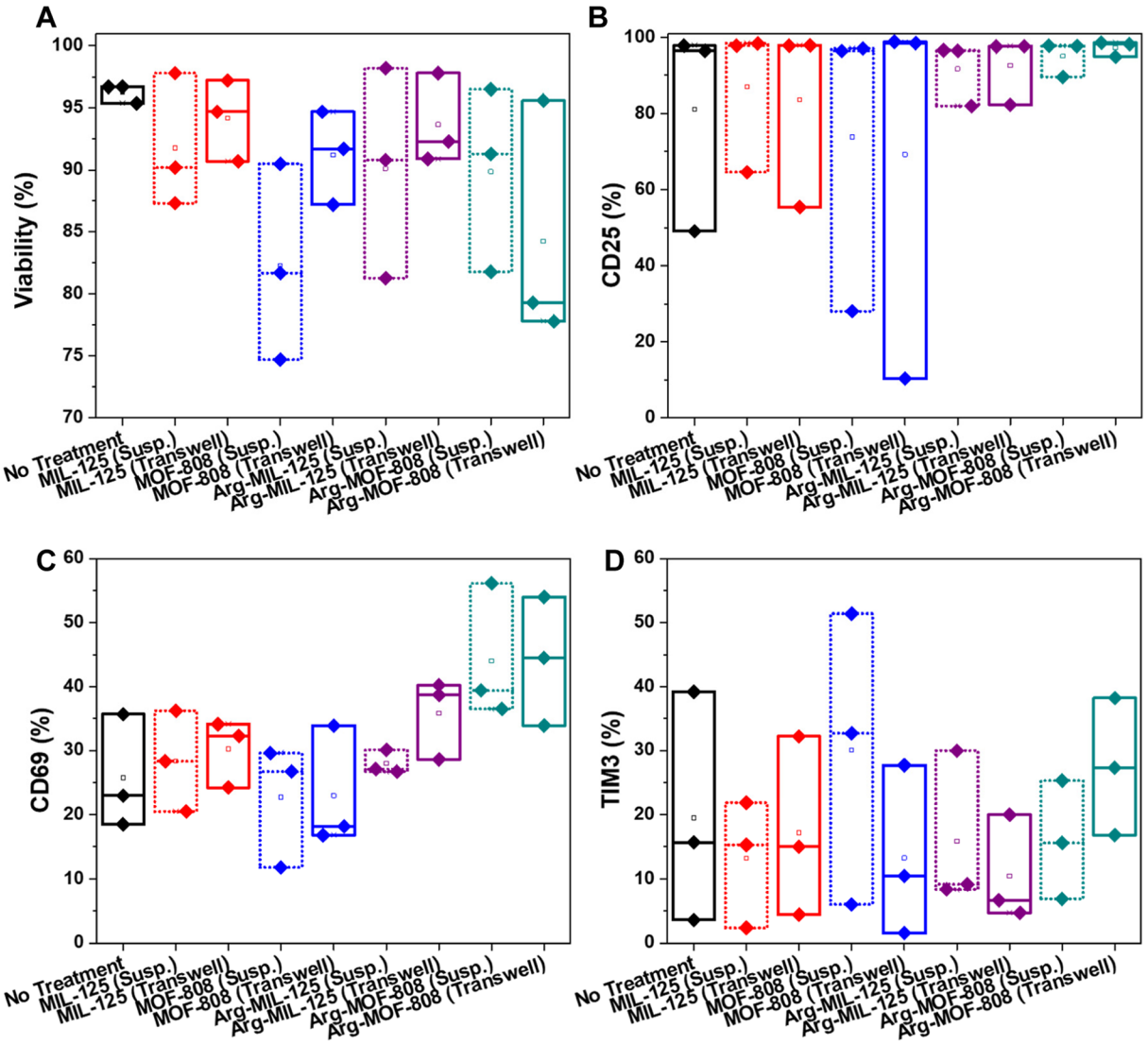

Fig. 3 Arg-loaded MOFs improve T-cell viability and preserve $CD4^+$ phenotype compared to unloaded nanoparticles. Flow cytometry analysis of Cell viability (A), CD25 (B), CD69 (C), and TIM-3 expression (D) after 72 h treatment with unloaded or Arg-loaded MOFs mixed with cells (Susp.) or seeded to transwells. Data are shown for three independent biological donors (n = 3). Each plotted point represents one donor with three technical replicates. Statistical analysis was performed using the Friedman test for repeated measures, with paired comparisons to untreated control shown as exploratory analyses.

press mitochondrial function. Thus, the improved viability and activation phenotype observed with arginine-loaded formulations is accompanied by enhanced bioenergetic capacity, linking carrier-mediated arginine delivery to both metabolic and functional reprogramming of T cells.

Overall, empty MOF-808 exerted the most pronounced negative effects on T-cell viability and activation, likely due to direct particle–cell interactions and impaired mitochondrial function. Arginine loading largely mitigated these effects and converted the formulation into a metabolically supportive and functionally activating carrier. NH_2-MIL-125 displayed better intrinsic biocompatibility and higher arginine loading capacity, but its Arg-loaded form induced a more metabolically intense response. Together, these findings show that MOF-mediated arginine delivery can reshape T-cell state in a formulation-dependent manner, with MOF-808 favouring a more balanced metabolic phenotype and NH_2-MIL-125 supporting stronger but potentially less restrained activation.

To further assess whether arginine delivery influenced T-cell phenotype beyond the activation markers analysed above, C–C chemokine receptor type 7 (CCR7) expression was examined in a follow-up experiment using an independent donor set and focusing on untreated control, soluble L-arginine, Arg-loaded NH_2-MIL-125, and Arg-loaded MOF-808 seeded to transwells. Across all groups, CCR7 expression remained consistently high, indicating that neither soluble arginine nor arginine-loaded MOFs caused a substantial loss of this marker (Fig. 4A). The highest and most uniform CCR7

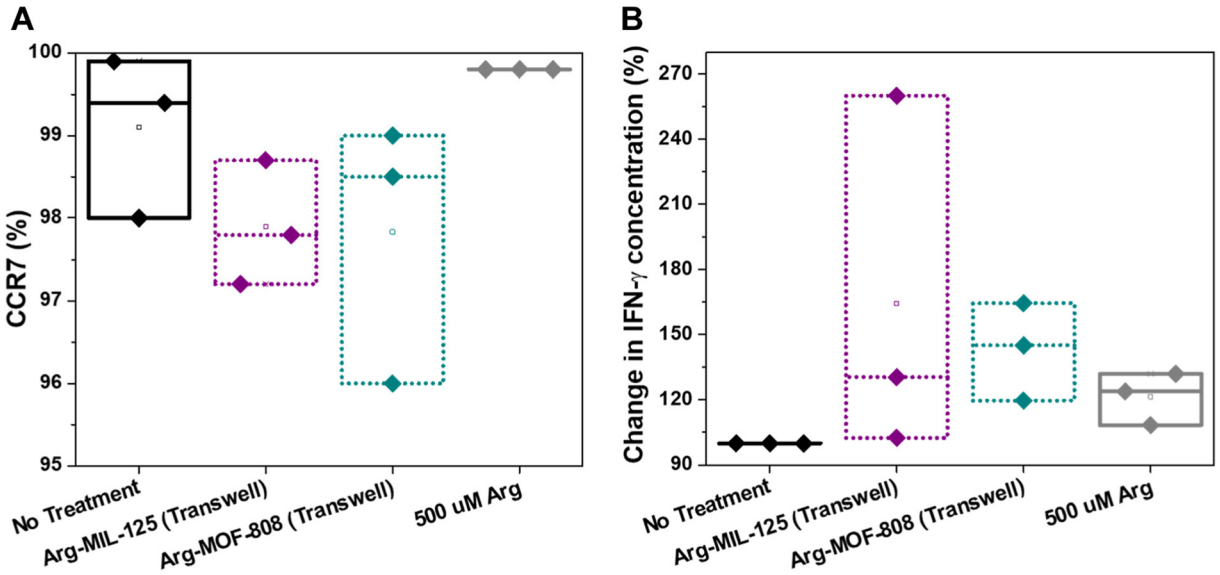

Fig. 4 CCR7 expression is maintained (A), while IFN-γ secretion shows a donor-dependent upward trend following treatment with arginine and arginine-loaded MOFs (B). Data are shown for three independent biological donors (n = 3). Each plotted point represents one donor with three technical replicates. Statistical analysis was performed using the Friedman test for repeated measures, with paired comparisons to untreated control shown as exploratory analyses.

levels were observed in the soluble arginine group, while both Arg-loaded MOF formulations also maintained CCR7 within a similarly high range, but with no significant differences between conditions. As CCR7 is a hallmark of central-memory and lymphoid-homing T cells, its preservation is generally associated with maintenance of a less differentiated phenotype rather than terminal effector polarization, as established in foundational studies of T-cell memory and more recent work showing that elevated intracellular arginine promotes a central-memory-like state with retention of CCR7 expression.[20,47] Thus, these findings suggest that arginine delivery, either in free form or *via* MOFs, does not adversely affect this memory-associated marker.

To complement this phenotypic analysis, IFN-γ secretion was quantified by ELISA under corresponding transwell conditions. In contrast to the relatively stable CCR7 profile, IFN-γ release showed clearer formulation-dependent differences. Arg-loaded NH_2-MIL-125 produced the most consistent increase in IFN-γ secretion across donors, while Arg-loaded MOF-808 also enhanced IFN-γ in two donors but showed greater donor-to-donor variability (Fig. 4B). However, no significant differences were detected between these conditions. Soluble 500 μM arginine increased IFN-γ relative to untreated controls in two donors, although this effect was less consistent overall. These findings are in line with the broader literature showing that arginine availability supports T-cell bioenergetics, survival, and activation, and can enhance effector responses including cytokine production, while the magnitude of this effect depends on the metabolic state of the cells and the mode of arginine delivery.[20,48] Taken together, these data indicate that arginine delivery can preserve CCR7 expression while modulating effector cytokine output in a carrier-dependent manner, with NH_2-MIL-125-based arginine delivery showing the most consistent association with preserved CCR7 expression and enhanced IFN-γ secretion across donors.

The metabolic effects observed following MOF-mediated arginine delivery are likely to reflect integration of nutrient-sensing and downstream functional pathways in activated T cells. Although mTOR signalling and other arginine-sensing mechanisms were not directly investigated in the present study, they represent plausible upstream regulators of the enhanced oxidative metabolism observed here. Importantly, the Seahorse findings were accompanied by changes in T-cell viability, activation-associated phenotypic markers, nitrite production, and IFN-γ secretion, indicating that arginine delivery influences not only mitochondrial respiration but also broader aspects of T-cell functional state. The nitrite data further suggest coupling between arginine availability and downstream nitrogen metabolism, although the present study does not establish whether the metabolic phenotype is directly dependent on ˙NO production. Future work should therefore examine mTOR-associated signalling, arginine transport/sensing pathways, and the causal contribution of ˙NO to the immunometabolic effects of these MOF formulations.

3.4. Modulation of iNOS-expressing MDA-MB-231 cells by Arg-releasing MOFs

3.4.1. Cell viability and cellular uptake of MOF nanoparticles. Having established that arginine-loaded MOFs differentially modulate T-cell metabolism and phenotype, we next examined whether the same delivery platforms could alter the behaviour of iNOS-expressing MDA-MB-231 cells. In this context, arginine delivery was expected to increase intracellular ˙NO generation through iNOS activity, thereby influencing

tumour-cell viability and migration. This complementary analysis was designed to determine whether framework-dependent arginine release could simultaneously support T-cell immunometabolism and modulate ˙NO-related tumour-cell responses in TNBC.

To mimic the pathophysiological microenvironment of breast cancer tissue, which is characterised by elevated iNOS expression and excessive ˙NO generation,[8,49] iNOS-transduced MDA-MB-231 cells were employed as previously described.[34] First, the metabolic activity of cells was assessed following exposure to free L-Arg in serum-free and serum-containing media to decouple the intrinsic biological effects of L-Arg from MOF-mediated delivery. Free L-Arg induced only modest and serum-dependent changes in metabolic activity, with attenuated effects observed in the presence of FBS, likely due to reduced cellular uptake and altered extracellular availability (Fig. S12). These findings highlight the limitations of soluble L-Arg administration and underscore the need for carrier-mediated delivery to enhance intracellular substrate availability for ˙NO production.

Next, to enable fluorescence-based tracking of nanoparticle internalisation, NH_2-MIL-125(Ti) and MOF-808(Zr) were loaded with the lipophilic fluorescent probe BODIPY™ 581/591 C11. Fluorescence emission was recorded between 591 and 599 nm following excitation at 581 nm to identify the optimal detection wavelength. Based on maximal fluorescence intensity and linearity of the standard curve, an emission wavelength of 595 nm was selected for all subsequent quantitative measurements. Fig. S13 shows the corresponding standard curve. Both frameworks exhibited comparable apparent loading capacities (0.69 ± 0.03% for BODIPY-NH_2-MIL-125 and 0.76 ± 0.01% for BODIPY–MOF-808) and high loading efficiencies (63.17 ± 2.62% and 69.34 ± 0.61%, respectively), confirming effective dye incorporation into both MOF carriers. Minimal dye release was observed upon suspension in PBS for 1 h, with no detectable BODIPY release from BODIPY–MIL-125 and only a trace amount released from BODIPY–MOF-808 (0.25 ± 0.02 μg), indicating stable probe retention under physiological conditions. These results confirm that the fluorescent signal used for subsequent uptake studies predominantly reflects nanoparticle-associated BODIPY rather than free dye, thereby providing a reliable basis for evaluating cellular internalisation.

Next, the cellular uptake of both BODIPY-labelled NH_2-MIL-125 and BODIPY-labelled MOF-808 particles was studied in FBS-free medium to maximize nanoparticle uptake and simplify fluorescence readouts. We also performed parallel tests in FBS-containing medium (data not shown), which as expected yielded lower uptake; this approach follows common practice since serum proteins bind nanoparticles and reduce apparent internalization.[50] For example, others have pre-incubated cells in FBS-free medium before applying MOFs and then measured uptake by flow cytometry.[51] In line with these reports, we found that adding FBS at 10% dramatically decreased the internalized signal. Prior studies similarly show that serum (FBS) induces MOF aggregation and protein corona formation; for instance, Hidalgo *et al.* reported that nanoMOFs in FBS-supplemented medium swelled in size and aggregated, altering their cellular uptake.[52] Likewise, Gan *et al.* observed that once a protein corona was formed (≥10% FBS), further increases in serum (to 20%) did not significantly change uptake.[53] Hence, focusing on FBS-free conditions aligns with the literature and allows us to isolate the intrinsic uptake behaviour of our BODIPY-labelled MOFs.

To account for potential spectral crosstalk from green fluorescent protein (GFP)-expressing MDA-MB-231 cells, we implemented rigorous fluorescence compensation and controls. Cells, treated with BODIPY™ 581/591 C11 alone at varying concentrations and in different media conditions, were used to establish compensation matrices by tracking red and green fluorescence over time (Fig. S14A, B and Videos S1–S3). Additional controls included untreated GFP-positive cells (to establish baseline autofluorescence; Video S4) and MOF samples in medium without cells (to account for extracellular fluorescence or surface-adsorbed signal). These data informed a 3% spillover correction from green to red, which was systematically applied to all subsequent analyses.

Fig. S15 shows the red fluorescence signal from BODIPY™ 581/591-loaded NH_2-MIL-125 and MOF-808 nanoparticles incubated in FBS-free medium without cells over 24 hours. For MIL-125, red fluorescence intensity steadily declined across all concentrations, likely reflecting gradual dye release and quenching in the extracellular environment (Fig. S15A and Videos S5–S7). In contrast, BODIPY-MOF-808 samples showed relatively stable or slightly increasing red signal over time, especially at higher concentrations, suggesting stronger dye retention or slower release from MOF-808 (Fig. S15B and Videos S8–S10). These measurements establish baseline dye behaviour in cell-free conditions, critical for interpreting cellular uptake experiments.

Upon incubation with iNOS-transduced MDA-MB-231 cells, distinct patterns emerged. For cells treated with BODIPY-loaded NH_2-MIL-125 nanoparticles, the red fluorescence (Fig. 5A and Videos S11–S13), which corresponds to the reduced, unoxidized form of BODIPY, decreased sharply within the first few hours, particularly at higher nanoparticle concentrations, suggesting rapid cellular uptake followed by intracellular oxidation of the probe. Concurrently, the green fluorescence (Fig. 5B), indicative of oxidized BODIPY, increased in a dose-dependent manner, peaking at 8 hours post-treatment and stabilizing thereafter. The temporal inverse trend of red and green signals confirms successful internalization of NH_2-MIL-125 and oxidation of the encapsulated probe, consistent with intracellular reactive oxygen species (ROS) and reactive nitrogen species (RNS) activity. These data support the use of BODIPY-loaded NH_2-MIL-125 as a reporter for oxidative processes in engineered tumour cells and demonstrate its responsiveness to redox conditions in live-cell assays.

A more pronounced response was observed with BODIPY-loaded MOF-808 nanoparticles. The red fluorescence (Fig. 5E and Videos S14–S16), showed an initial rise followed by a gradual decline, with peak intensities increasing in a concentration-dependent manner, indicating nanoparticle uptake

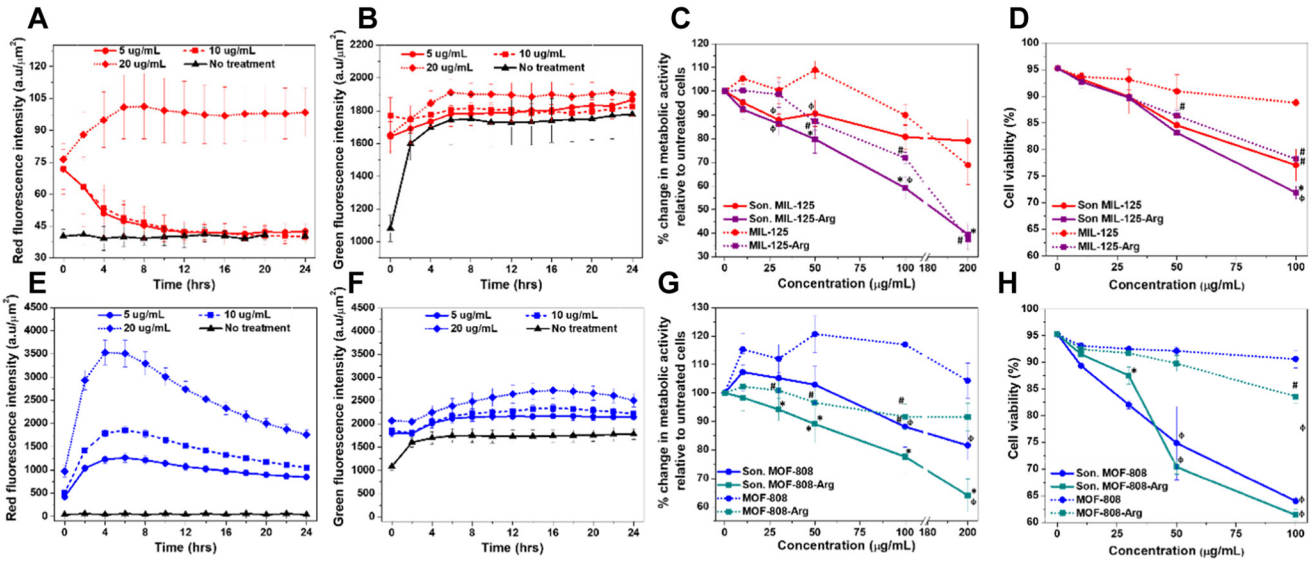

Fig. 5 Cellular uptake and viability of MDA-MB-231(iNOS) cells treated with BODIPY-labeled or Arg-loaded MOFs. (A, B, E and F) Time-resolved red (A and E) and green (B and F) fluorescence in cells treated with BODIPY™ 581/591 C11-labeled NH_2-MIL-125 (A and B) or MOF-808 nanoparticles (E and F) in FBS-free medium. (C and D) Metabolic activity and viability of cells treated with NH_2-MIL-125, either unloaded or Arg-loaded, with or without prior sonication. (G and H) Metabolic activity and viability of cells treated with MOF-808 nanoparticles under the same conditions. Data represent mean ± SD from $n = 3$ independent experiments. Statistical significance was determined using a two-tailed unpaired t-test: $^{*}p < 0.05$ for loaded *vs.* unloaded sonicated MOFs; $^{\#}p < 0.05$ for loaded *vs.* unloaded MOFs; $^{\Phi}p < 0.05$ for sonicated *vs.* unsonicated MOFs.

and intracellular delivery of the dye. The green fluorescence (Fig. 5F), increased progressively over time in treated cells, most notably at the highest concentration, suggesting active intracellular oxidation likely mediated by ˙NO or ROS/RNS activity. While the green signal increase was moderate compared to that observed with MIL-125, it remained above control throughout, confirming redox-responsive oxidation. Together, these results confirm cellular uptake of MOF-808 and release of the encapsulated probe, albeit with slightly delayed or less intense oxidation kinetics than MIL-125, possibly due to differences in particle internalization rate or redox reactivity.

In parallel, the concentration-dependent effects of NH_2-MIL-125(Ti) and MOF-808(Zr) on the metabolic activity of iNOS-expressing MDA-MB-231 cells were evaluated in both serum-free and serum-containing media. The two frameworks exhibited distinct cytocompatibility profiles, which were strongly influenced by medium composition (Fig. S16A and B). Furthermore, metal release/degradation measurements provide an initial indication of framework lability and potential exposure to Ti- or Zr-containing species (Fig. 1A and B). Under serum-free conditions, NH_2-MIL-125 caused a greater reduction in metabolic activity compared with MOF-808, consistent with previous reports indicating that zirconium–carboxylate frameworks such as MOF-808 generally display higher biocompatibility,[54] whereas titanium-based MOFs may exert moderate cytotoxic effects at elevated concentrations.[55] Importantly, no interference of the MOF nanoparticles with the AlamarBlue™ assay was detected under the experimental conditions used.

The inclusion of 10% FBS markedly attenuated the cytotoxic effects of both MOFs. This effect is attributed to protein corona formation, whereby adsorbed serum proteins alter nanoparticle surface properties, reduce cellular uptake, and limit direct membrane interactions.[56,57] This serum-dependent modulation highlights the critical role of nanoparticle–biomolecule interactions in governing cellular responses. Consequently, subsequent functional assays were conducted under serum-free conditions to minimise protein corona formation and enable direct evaluation of the biological effects arising from L-Arg release from the MOF carriers. This experimental design is consistent with standard protocols used for intracellular ˙NO measurements and migration assays.

Both NH_2-MIL-125(Ti) and MOF-808(Zr) nanoparticles exhibited a significant reduction in the metabolic activity of MDA-MB-231(iNOS) cells upon L-Arg loading compared with their unloaded counterparts (Fig. 5C and G). In iNOS-overexpressing cells, MOF-mediated delivery of L-Arg supplies excess substrate for ˙NO synthesis, thereby amplifying intracellular ˙NO production. Elevated ˙NO levels are known to promote apoptotic signalling and suppress proliferation in cancer cells,[58,59] consistent with the pronounced decrease in metabolic activity observed following treatment with Arg-loaded MOFs. Sonication further enhanced the cytotoxic efficacy of both MOF systems. Sonicated nanoparticles (Son) induced a significantly stronger reduction in metabolic activity than their non-sonicated counterparts (ϕ), as shown in Fig. 5D and H. This enhancement is attributed to improved dispersion and reduced aggregation following sonication, resulting in increased colloidal stability and more efficient cellular

uptake.[60] Consequently, intracellular delivery of encapsulated L-Arg was enhanced, leading to greater suppression of cellular metabolic activity.

Together, these data support the short-term *in vitro* tolerability of the platforms under the tested conditions, while also showing that safety is material- and context-dependent. However, the identity and biological effects of long-term degradation products, as well as the consequences of chronic metal ion exposure, remain to be established in dedicated long-term and *in vivo* studies.

3.4.2. Detection of intracellular ˙NO. Intracellular ˙NO production was quantified using the DAF-FM fluorescent probe in iNOS-expressing MDA-MB-231 cells to assess the functional delivery of L-Arg from MOF carriers. Treatment with Arg-loaded MOFs resulted in a marked increase in fluorescence intensity compared to that of unloaded controls, confirming that the released L-Arg enhanced iNOS-mediated ˙NO synthesis. Among the formulations, Arg–MOF-808 consistently induced higher fluorescence than its unloaded counterpart, whereas the enhancement observed with Arg–MIL-125 was comparatively modest (Fig. 6A and B).

Sonication further amplified the intracellular ˙NO response, particularly for Arg–MIL-125, which exhibited the earliest and most pronounced ˙NO burst. At 4 h, fluorescence in cells treated with sonicated Arg–MIL-125 was approximately 3.2-fold higher than that of sonicated unloaded MIL-125, while the difference between Arg-loaded and unloaded MOF-808 was around 1.4-fold. Under non-sonication conditions, Arg–MOF-808 outperformed Arg–MIL-125. Over prolonged incubation (12–24 h), MOF-808 sustained higher intracellular ˙NO levels; at 12 h, fluorescence in Arg–MIL-125-treated cells reached 16 ± 1.7 arbitrary units (a.u). *versus* 5 ± 0.2 a.u. for the unloaded framework, whereas Arg–MOF-808 achieved 2.5 ± 0.3 a.u. compared to 1.0 ± 0.2 a.u. for its unloaded form. Videos S17–24 show the time-lapse fluorescence images of ˙NO generation in response to different nanoparticles, compared to the untreated cells.

Overall, Arg–MOF-808 generated significantly more sustained ˙NO than MIL-125 ($p < 0.01$, 6–12 h), whereas sonication primarily accelerated the early release peak without altering the total cumulative ˙NO output. Although sonicated MOF-808 nanoparticles appeared to cause minor interference in fluorescence readings, the substantial increase observed with Arg–MOF-808 confirms that the enhanced signal reflects genuine intracellular ˙NO production rather than optical artifacts. These ˙NO-release profiles closely aligned with the arginine-release kinetics, wherein MIL-125 exhibited a slower, diffusion-controlled release, whereas MOF-808 enabled faster and more sustained substrate delivery. Collectively, DAF-FM data demonstrated that Arg loading markedly enhanced iNOS-dependent ˙NO generation in cancer cells, with MOF-808 providing a more stable and prolonged intracellular ˙NO signal, especially following sonication. The time course ˙NO generation in L-Arg-treated cells is shown in Fig. S17. These results indicate that the Arg-loaded MOFs, provides significantly more potent and sustained ˙NO delivery than free L-Arg, especially when sonicated. This sustained intracellular ˙NO is crucial for therapeutic applications, and DAF-FM imaging here effectively captures the differences in kinetic profile and delivery performance between the two approaches.

3.4.3. Cell migration. To evaluate the influence of the released therapeutic gas on cancer cell migration, a scratch (wound healing) assay was performed using MDA-MB-231(iNOS) cells cultured in the absence of direct nanoparticle contact. This setup enabled the assessment of the effects of the released L-Arg, and downstream ˙NO production on wound closure dynamics, independent of direct nanoparticle–cell contact. Among all formulations, MIL-125-Arg exhibited the strongest inhibition of migration, followed by MOF-808-Arg, indicating that arginine delivery *via* MOFs effectively suppresses migration, likely through elevated sustained ˙NO production (Fig. 6C and Videos S25–S30). These findings underscore the dominant role of MOF-mediated arginine delivery and subsequent ˙NO generation in limiting cancer cell motility.

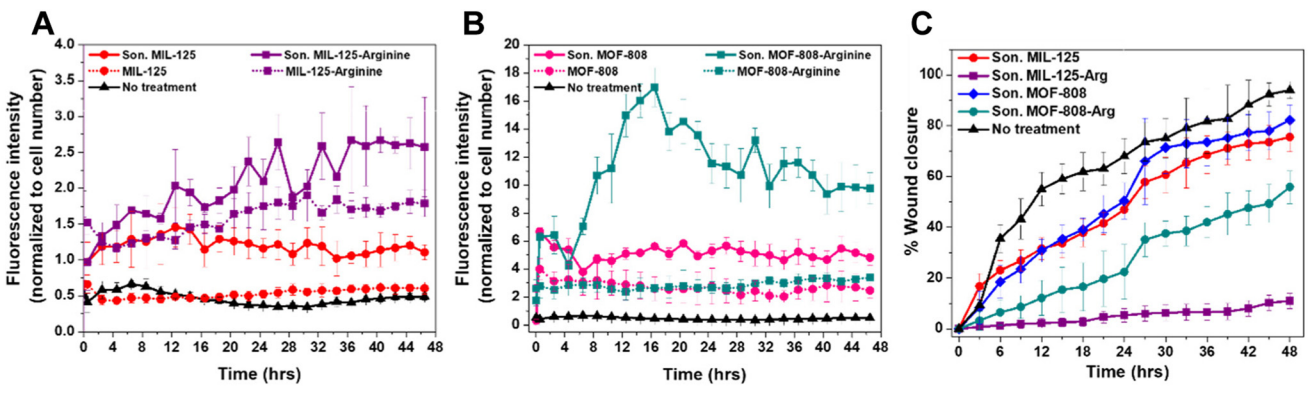

Fig. 6 Arg-loaded MOFs enhance intracellular ˙NO generation in iNOS-expressing MDA-MB-231 cells and inhibit their migration. (A and B) Time-dependent intracellular ˙NO production in cells treated with sonicated or unsonicated NH_2-MIL-125 (A) and MOF-808 (B) nanoparticles, either unloaded or loaded with L-Arg. (C) Percentage of wound closure over time in cells treated with unloaded or Arg-loaded NH_2-MIL-125 and MOF-808 nanoparticles. Data represent mean ± SD from $n = 3$ independent experiments.

This pronounced inhibition by Arg-loaded MOFs is consistent with the established cytostatic and antimigratory effects of high ˙NO concentrations. L-Arg serves as a substrate for iNOS, and its excess drives elevated ˙NO generation. While low ˙NO levels (nanomolar range) promote tumour cell survival and migration, high ˙NO fluxes (micromolar range) induce oxidative and nitrosative stress, DNA damage, and apoptosis.[6,7] Comparable observations have been reported in other cancer models as well. For instance, it was demonstrated that the overexpression of argininosuccinate synthetase in hepatocellular carcinoma cells, leading to elevated intracellular arginine levels, suppressed wound healing and metastasis.[61] Similarly, nanoscale ˙NO delivery *via* lipid–PLGA nanoparticles reprograms the tumour microenvironment toward an immunostimulatory phenotype, inhibiting metastasis *in vivo*.[62]

Our findings align with these reports: Arg-loaded MOFs likely provided a burst of substrate to iNOS, generating a transient but intense ˙NO flux that suppressed migration. The concentration-dependent behaviour of ˙NO explains this effect: low ˙NO supports PI3K/Akt and HIF-1α pathways to promote survival and migration, whereas sustained high ˙NO in serum-free conditions overwhelms these signals, leading to cytostasis. In our serum-free assay setting, rapid arginine-release probably triggered a high ˙NO peak that transiently arrested cell motility, consistent with previous findings where fast-degrading ˙NO donors inhibited migration in FBS-free media.[63] The MOF scaffolds may have contributed by locally concentrating arginine and facilitating localized ˙NO generation. Moreover, MOFs at the nanoscale can enhance intracellular uptake and, under certain conditions, generate reactive species,[64] which might further potentiate this effect, although this mechanism was not explored in this study.

Together, these data show that NH_2-MIL-125 and MOF-808 act as active arginine carriers in iNOS-expressing TNBC cells, enhancing intracellular ˙NO-associated responses and reducing migration, while also modulating T-cell metabolic fitness. Viewed alongside the T-cell findings, this supports a dual biological role for MOF-mediated arginine delivery, in which the overall outcome depends not only on cargo identity but also on carrier-dependent release behaviour and the metabolic context of the target cell. The two frameworks therefore provide distinct yet complementary delivery profiles that influence both immune and tumour-cell behaviour within the TNBC microenvironment. As these findings are based on *in vitro* models, future studies will assess pharmacokinetics, biodistribution, and safety in orthotopic TNBC models to establish translational relevance.

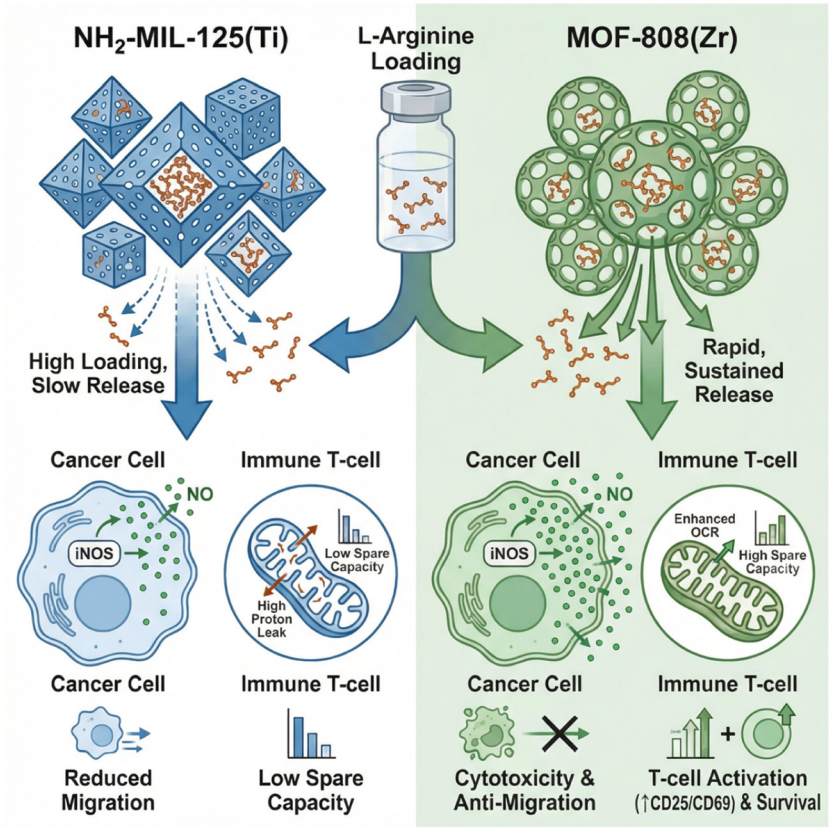

Scheme 2 Schematic comparison of Arg-loaded NH_2-MIL-125 and MOF-808 nanoparticles and their distinct biological effects. Illustration highlights differences in pore structure, L-Arg release kinetics, and subsequent outcomes in T cells (metabolic reprogramming and activation) and cancer cells (NO-mediated cytotoxicity and migration inhibition). Created by illustrae.co.

4. Conclusion

This study establishes NH_2-MIL-125(Ti) and MOF-808(Zr) as tunable arginine nanocarriers for coordinated modulation of tumour and immune-cell behaviour in TNBC. The two frameworks exhibited distinct physicochemical properties, with NH_2-MIL-125 showing higher arginine loading capacity and more sustained release, while MOF-808 displayed faster release and greater colloidal stability in biologically relevant media. These delivery differences translated into markedly different biological responses. In activated human T cells, Arg-loaded MOFs restored mitochondrial respiration relative to unloaded carriers and induced formulation-dependent immunometabolic phenotypes. NH_2-MIL-125-Arg drove a stronger but less regulated respiratory response characterized by elevated proton leak and loss of spare respiratory capacity, whereas MOF-808-Arg supported a more balanced bioenergetic profile. Flow-cytometry, follow-up CCR7 analysis, and IFN-γ measurements further showed that arginine delivery influenced T-cell viability, activation state, and cytokine output in a carrier-dependent manner. In parallel, both Arg-loaded MOFs enhanced intracellular $^{\bullet}$NO-associated responses in iNOS-expressing MDA-MB-231 cells and inhibited tumour-cell migration, supporting their role as functional substrate-delivery systems in the TNBC setting. These differences are summarized in Scheme 2. Collectively, these findings show that MOF-mediated arginine delivery is not merely a strategy for amplifying tumour-cell $^{\bullet}$NO production, but a broader platform for coordinated tumour–immune metabolic modulation. By linking carrier chemistry to release kinetics, T-cell bioenergetics, and tumour-cell behaviour, this work provides a foundation for future development of nutrient-delivery biomaterials for metabolically hostile cancers. Further studies should define the underlying arginine-sensing pathways in immune cells, clarify long-term degradation and safety profiles, and evaluate therapeutic efficacy *in vivo*.

Author contributions

Amir Alsharabasy: data curation (lead), formal analysis (lead), investigation (lead), methodology (lead), validation (lead), writing – original draft (lead), writing – review & editing (supporting). Aibhe Boran: data curation (supporting), methodology (supporting), formal analysis (supporting), investigation (supporting). Roberto González-Gómez: data curation (supporting), methodology (supporting), formal analysis (supporting), investigation (supporting), writing – original draft (supporting). Harry Revill: data curation (supporting), methodology (supporting), formal analysis (supporting). Abhay Pandit: conceptualization (equal), funding acquisition (lead), supervision (lead), writing – review & editing (lead). Pau Farràs: conceptualization (equal), funding acquisition (lead); supervision (lead), writing – review & editing (lead).

Conflicts of interest

The authors declare no conflict of interest.

Data availability

The data supporting this article have been included as part of the supplementary information (SI). Supplementary information is available. See DOI: https://doi.org/10.1039/d6bm00195e.

Acknowledgements

We acknowledge the research grant from Research Ireland co-funded under the European Regional Development Fund (Grant number 13/RC/2073_P2). A. A. acknowledges funding support from the Irish Research Council (Grant number GOIPD/2023/1640). A. B. acknowledges funding support from the Irish Research Council (GOIPG/2025/8895). H. R. acknowledges MedDevDoc, Co-funded by the European Union's Marie Skłodowska-Curie Actions (MSCA) programme under Grant Agreement 101126640.

References

1 C. Nathan and Q.-w. Xie, *Cell*, 1994, **78**, 915–918.
2 S. W. Ryter and A. M. K. Choi, *Am. J. Respir. Cell Mol. Biol.*, 2009, **41**, 251–260.
3 D. Fukumura, S. Kashiwagi and R. K. Jain, *Nat. Rev. Cancer*, 2006, **6**, 521–534.
4 H. Cheng, L. Wang, M. Mollica, A. T. Re, S. Wu and L. Zuo, *Cancer Lett.*, 2014, **353**, 1–7.
5 P. Fagone, E. Mazzon, P. Bramanti, K. Bendtzen and F. Nicoletti, *Eur. J. Pharmacol.*, 2018, **834**, 92–102.
6 A. J. Burke, F. J. Sullivan, F. J. Giles and S. A. Glynn, *Carcinogenesis*, 2013, **34**, 503–512.
7 A. M. Alsharabasy, S. A. Glynn and A. Pandit, *Biochem. Soc. Trans.*, 2020, **48**, 2539–2555.
8 P. Garrido, A. Shalaby, E. M. Walsh, N. Keane, M. Webber, M. M. Keane, F. J. Sullivan, *et al.*, *Oncotarget*, 2017, **8**, 80568–80588.
9 A. M. Alsharabasy, A. Aljaabary, R. Bohara, P. Farràs, S. A. Glynn and A. Pandit, *ACS Pharmacol. Transl. Sci.*, 2023, **6**, 1416–1432.
10 M. Lahiri and J. H. J. Martin, *Oncol. Rep.*, 2009, **21**, 275–281.
11 S. Kashiwagi, K. Tsukada, L. Xu, J. Miyazaki, S. V. Kozin, J. A. Tyrrell, W. C. Sessa, *et al.*, *Nat. Med.*, 2008, **14**, 255–257.
12 K. M. Miranda, L. A. Ridnour, C. L. McGinity, D. Bhattacharyya and D. A. Wink, *Inorg. Chem.*, 2021, **60**, 15941–15947.
13 K.-D. Kröncke and C. V. Suschek, *J. Invest. Dermatol.*, 2008, **128**, 258–260.
14 J. A. Hrabie and L. K. Keefer, *Chem. Rev.*, 2002, **102**, 1135–1154.
15 S. Bodeboger, F. Scalera and L. Ignarro, *Pharmacol. Ther.*, 2007, **114**, 295–306.

16 K. Zhang, H. Xu, X. Jia, Y. Chen, M. Ma, L. Sun and H. Chen, *ACS Nano*, 2016, **10**, 10816–10828.
17 S.-S. Wan, J.-Y. Zeng, H. Cheng and X.-Z. Zhang, *Biomaterials*, 2018, **185**, 51–62.
18 V. Bronte and P. Zanovello, *Nat. Rev. Immunol.*, 2005, **5**, 641–654.
19 P. C. Rodriguez, D. G. Quiceno and A. C. Ochoa, *Blood*, 2007, **109**, 1568–1573.
20 R. Geiger, J. C. Rieckmann, T. Wolf, C. Basso, Y. Feng, T. Fuhrer, M. Kogadeeva, P. Picotti, F. Meissner, M. Mann, N. Zamboni, F. Sallusto and A. Lanzavecchia, *Cell*, 2016, **167**, 829–842.
21 H. B. Ji, S.-N. Kim, C. R. Kim, C. H. Min, J. H. Han, M. J. Kim, C. Lee and Y. B. Choy, *Biomater. Adv.*, 2023, **145**, 213268.
22 R. Chaudhari, V. Patel and A. Kumar, *Nanoscale Adv.*, 2024, **6**, 2270–2286.
23 X.-R. Jiang, J. Mi, Y. Wang, M. Yin, Y. Tong and Y. Zhu, *Int. J. Nanomed.*, 2025, **20**, 10127–10149.
24 S. Kulkarni, S. Soman, A. Pandey and S. Mutalik, *Int. J. Biol. Macromol.*, 2025, **322**, 146857.
25 S. Zhou, Q. Shang, J. Ji and Y. Luan, *ACS Appl. Mater. Interfaces*, 2021, **13**, 47407–47417.
26 F. D. Duman, A. Monaco, R. Foulkes, C. R. Becer and R. S. Forgan, *ACS Appl. Nano Mater.*, 2022, **5**, 13862–13873.
27 A. Kazemi, H. A. M. Aliabadi, M. H. Afshari, M. Tamtaji, H. Baesmat, S. Keshavarz, F. Zeinali, *et al.*, *ACS Appl. Bio Mater.*, 2025, **8**, 7830–7841.
28 A. Rengaraj, P. Puthiaraj, N.-S. Heo, H. Lee, S. K. Hwang, S. Kwon, W.-S. Ahn and Y.-S. Huh, *Colloids Surf., B*, 2017, **160**, 1–10.
29 M. Bagherzadeh, M. Safarkhani, M. Kiani, F. Radmanesh, H. Daneshgar, A. M. Ghadiri, F. Taghavimandi, *et al.*, *Sci. Rep.*, 2022, **12**, 12105.
30 G. Wen and Z. Guo, *Colloids Surf., A*, 2018, **541**, 58–67.
31 J. Y. Oh, E. Choi, B. Jana, E. M. Go, E. Jin, S. Jin, J. Lee, *et al.*, *Small*, 2023, **19**, 2300218.
32 X. Yin, S. Xue, J. Ji, M. Zhao, M. Shao, L. Yin, S. Zhang, *et al.*, *Adv. Compos. Hybrid Mater.*, 2025, **8**, 332.
33 A. C. Staußß, C. Fuchs, P. Jansen, S. Repert, K. Alcock, S. Ludewig and W. Rozhon, *Molecules*, 2024, **29**, 3262.
34 A. M. Alsharabasy, D. Cherukaraveedu, J. Warneke, Z. Warneke, J. R. Galán-Mascarós, S. A. Glynn, P. Farràs and A. Pandit, *Small Sci.*, 2024, **4**, 2400237.
35 A. Ahmed, C. G. Efthymiou, R. Sanii, E. Patyk-Kazmierczak, A. M. Alsharabasy, M. Winterlich, N. Kumar, *et al.*, *J. Mater. Chem. B*, 2022, **10**, 1378–1385.
36 B. Möller, M. Glaß, D. Misiak and S. Posch, *J. Open Res. Softw.*, 2016, **4**, 17.
37 M. Rath, I. Müller, P. Kropf, E. I. Closs and M. Munder, *Front. Immunol.*, 2014, **5**, 532.
38 Z. V. Kuropteva, L. M. Baider, L. G. Nagler, T. N. Bogatyrenko and O. L. Belaia, *Russ. Chem. Bull.*, 2019, **68**, 174–180.
39 H. Furukawa, F. Gándara, Y.-B. Zhang, J. Jiang, W. L. Queen, M. R. Hudson and O. M. Yaghi, *J. Am. Chem. Soc.*, 2014, **136**, 4369–4381.
40 J. H. Cavka, S. Jakobsen, U. Olsbye, N. Guillou, C. Lamberti, S. Bordiga and K. P. Lillerud, *J. Am. Chem. Soc.*, 2008, **130**, 13850–13851.
41 S. Yuan, J. Peng, Y. Zhang and Y. Shao-Horn, *J. Phys. Chem. C*, 2019, **123**, 28266–28274.
42 C. Păun, L. Motelică, D. Ficai, A. Ficai and E. Andronescu, *Materials*, 2023, **16**, 6143.
43 S. Vilela, P. Salcedo-Abraira, I. Colinet, F. Salles, M. De Koning, M. Joosen, C. Serre and P. Horcajada, *Nanomaterials*, 2017, **7**, 321.
44 P. C. Rodriguez, D. G. Quiceno, J. Zabaleta, B. Ortiz, A. H. Zea, M. B. Piazuelo, A. Delgado, P. Correa, J. Brayer, E. M. Sotomayor, S. Antonia, J. B. Ochoa and A. C. Ochoa, *Cancer Res.*, 2004, **64**, 5839–5849.
45 A. H. Zea, P. C. Rodriguez, K. S. Culotta, C. P. Hernandez, J. DeSalvo, J. B. Ochoa, H.-J. Park, J. Zabaleta and A. C. Ochoa, *Cell. Immunol.*, 2004, **232**, 21–31.
46 A.-A. M. Líndez, I. Dunand-Sauthier, M. Conti, F. Gobet, N. Núñez, J. T. Hannich, H. Riezman, R. Geiger, A. Piersigilli, K. Hahn, S. Lemeille, B. Becher, T. De Smedt, S. Hugues and W. Reith, *JCI Insight*, 2019, **4**, e132975.
47 F. Sallusto, D. Lenig, R. Förster, M. Lipp and A. Lanzavecchia, *Nature*, 1999, **402**, 34–38.
48 H. Shi, N. M. Chapman, J. Wen, C. Guy, L. Long, Y. Dhungana, S. Rankin, S. Pelletier, P. Vogel, H. Wang, J. Peng, K.-L. Guan and H. Chi, *Immunity*, 2019, **51**, 1012–1027.
49 W. Tschugguel, C. Schneeberger, G. Unfried, K. Czerwenka, W. Weninger, M. Mildner, D. M. Gruber, *et al.*, *Breast Cancer Res. Treat.*, 1999, **56**, 143–149.
50 E. Linnane, S. Haddad, F. Melle, Z. Mei and D. Fairen-Jimenez, *Chem. Soc. Rev.*, 2022, **51**, 6065–6086.
51 Z. He, Z. Liu, Y. Zhang, T. Guo and N. Feng, *J. Nanobiotechnol.*, 2025, **23**, 118.
52 T. Hidalgo, M. Alonso-Nocelo, B. L. Bouzo, S. Reimondez-Troitiño, C. Abuin-Redondo, M. de la Fuente and P. Horcajada, *Nanoscale*, 2020, **12**, 4839–4845.
53 N. Gan, Q. Sun, L. Zhao, P. Tang, Z. Suo, S. Zhang, Y. Zhang, M. Zhang, W. Wang and H. Li, *Int. J. Biol. Macromol.*, 2019, **140**, 709–718.
54 P. Wiśniewska, J. Haponiuk, M. R. Saeb, N. Rabiee and S. A. Bencherif, *Chem. Eng. J.*, 2023, **471**, 144400.
55 M. Safarkhani, A. Ojaghi, S. M. Nezhad, H. Daneshgar, A. C. Paiva-Santos, F. Radmanesh, M. Bagherzadeh, *et al.*, *Adv. Compos. Hybrid Mater.*, 2024, **7**, 18.
56 G. Duan, S.-g. Kang, X. Tian, J. A. Garate, L. Zhao, C. Ge and R. Zhou, *Nanoscale*, 2015, **7**, 15214–15224.
57 D. P. Mitev, A. M. Alsharabasy, L. Morrison, S. Wittig, C. Diener and A. Pandit, *Front. Bioeng. Biotechnol.*, 2021, **9**, 637587.
58 R. Singh, S. Pervin, A. Karimi, S. Cederbaum and G. Chaudhuri, *Cancer Res.*, 2000, **60**, 3305–3311.
59 J. L. Gordon, K. J. Hinsen, M. M. Reynolds and M. A. Brown, *Diseases*, 2021, **9**, 82.
60 Y. Sun, L. Zheng, Y. Yang, X. Qian, T. Fu, X. Li, Z. Yang, *et al.*, *Nano-Micro Lett.*, 2020, **12**, 103.

61 H. S. Eun, *J. Liver Cancer*, 2025, **25**, 1–3.
62 Y.-C. Sung, P.-R. Jin, L.-A. Chu, F.-F. Hsu, M.-R. Wang, C.-C. Chang, S.-J. Chiou, *et al.*, *Nat. Nanotechnol.*, 2019, **14**, 1160–1169.
63 A. M. Alsharabasy, S. Glynn, P. Farràs and A. Pandit, *Biomacromolecules*, 2022, **23**, 3621–3647.
64 K. Ni, G. Lan and W. Lin, *ACS Cent. Sci.*, 2020, **6**, 861–868.